J. Fluid Mech. (1990), *vol.* 215, *pp.* 365–391
Printed in Great Britain

An experimental investigation of turbulent shear flow cavitation

By T. J. O'HERN[†]

Fluid and Thermal Sciences Department, Sandia National Laboratories,
Albuquerque, NM 87185, USA

(Received 1 January 1989 and in revised form 28 October 1989)

Cavitation inception in a turbulent shear layer was studied at Reynolds numbers up to 2×10^6. Flash photography, high-speed motion pictures and holography were used to study the relation of cavitation inception to the shear-layer turbulent structure. Both spanwise and streamwise vortices were clearly visualized by the cavitation. Cavitation inception consistently occurred in the streamwise vortices and more fully developed cavitation was visible in both structures, with the streamwise cavities typically confined to the braid regions between adjacent spanwise vortices. The strength of the streamwise vortices was estimated using a Rankine vortex model, which showed that their strength was always less than 10% of that of the spanwise vortices. Measurements of fluctuating pressures were made by holographically monitoring the size of air bubbles injected into the non-cavitating shear flow. The measured pressure fluctuations had positive and negative peaks as high as 3 times the free-stream dynamic pressure, sufficient to explain cavitation inception at high values of the inception index. The occurrence of inception in the streamwise vortices of the shear layer, combined with previous reports of velocity dependence of the streamwise vortex strength, may explain the commonly observed Reynolds-number scaling of the cavitation inception index in shear flows.

1. Introduction

Despite their common occurrence in many cases of engineering importance, cavitation phenomena in turbulent shear flows have not been very extensively studied, for several reasons. First, the controlling features of the underlying single-phase flow have yet to be determined, remaining a topic of active research. Second, cavitation phenomena in shear flows are ill-suited to laboratory examination because of their commonly observed strong scaling, with scale effects generally much more significant than those associated with the flows around streamlined bodies. Inception indices for shear flows are usually considerably higher than those for flows around streamlined bodies; i.e. shear flows are typically more susceptible to cavitation. Unlike cavitation in flows around streamlined bodies, inception in shear flows occurs in the free stream, usually far from a test body, owing to the vortices and associated fluctuating pressure peaks in the shear layer.

Pioneering work on cavitation inception and scaling in turbulent shear flows was performed by Kermeen & Parkin (1957) in their study of the wake of sharp-edged disks, in which inception consistently occurred in the turbulent shear layer of the disk wake. Arndt (1978) made similar observations of the cavitating flow in the wake

---

[†] This work was performed in the Mechanical Engineering Department, California Institute of Technology, Pasadena, CA 91125, USA.

of sharp-edged disks. Katz (1984) studied the cavitating flows around blunt circular cylinders, and showed that inception occurred within the turbulent separated shear layer. Additional investigations into cavitation in turbulent shear flows include those of Van der Muelen (1980) of cavitation in the flow past hydrofoils at various angles of incidence, Ooi (1981, 1985) of scale effects in submerged water jets, and Franc & Michel (1983) on the effect of cavitation on vortex shedding in the wake of wedges.

1.1. *Turbulent structure of shear flows*

The organized vortical structure of plane two-stream mixing layers has been the topic of numerous investigations (e.g. Brown & Roshko 1974; Winant & Browand 1974; Dimotakis & Brown 1976). The existence of streamwise-oriented vortices as part of the shear-layer turbulent structure was suggested by Brown & Roshko (1974), and subsequent examinations of the coherent structure of plane mixing layers have provided a great deal more insight into this secondary structure. Bernal (1981) and Bernal & Roshko (1986) have demonstrated that the streamwise structure is composed of pairs of counter-rotating vortices. They developed a mixing-layer model in which the braid region between adjacent spanwise vortices contains an array of longitudinal vortices; each streamwise vortex being part of a continuous vortex line which snakes between neighbouring spanwise eddies, superimposed on the periphery of the primary structure in such a way that the basic coherence of the spanwise vortices is not destroyed. Lasheras, Cho & Maxworthy (1986) performed a low-Reynolds-number flow visualization study of a plane two-stream mixing layer and found that the first appearance of streamwise vortices always takes place in the braid regions. The data of Bernal (1981) and Lasheras *et al.* (1986) indicate that streamwise vortices are caused by shear-layer instability to upstream flow perturbations. Once formed, the instability waves are amplified by stretching in the braid region until they become strong enough for detection.

1.2. *Scope of the present work*

An experimental investigation into cavitation in the wake of a sharp-edged plate was performed in order to examine a turbulent shear layer in more detail than was possible in previous smaller scale experiments. The large physical dimension of the separated shear flow in the present study allowed detailed optical flow diagnostics. Specific examination was made of the relationship between cavitation phenomena and the shear-flow turbulent structure.

2. Experimental apparatus and techniques

Experiments were conducted in the California Institute of Technology low-turbulence water tunnel (LTWT). The rectangular test section is 2.5 m long and has a cross-section that expands from 0.3 by 0.3 m at the inlet to 0.3 by 0.36 m at the outlet, with the spanwise distance remaining constant. The test section is enclosed by glass side windows and Plexiglas top and bottom windows. The maximum unblocked test section velocity is 7.3 m/s. A low free-stream turbulence level of less than 0.04 % is maintained over the full tunnel velocity range (Gates 1977) through use of vaned turning elbows, a settling chamber containing honeycombs and screens, and a 16:1 contraction-ratio nozzle. A pressure control tank connected to a 5 HP vacuum pump allows control of tunnel mean static pressure from 0.1 atm to 1.2 atm. The LTWT does not contain a resorber, and at maximum velocity the water recirculation time is about 30 s. Nuclei control is achieved through filtration and deaeration (Ooi 1981).

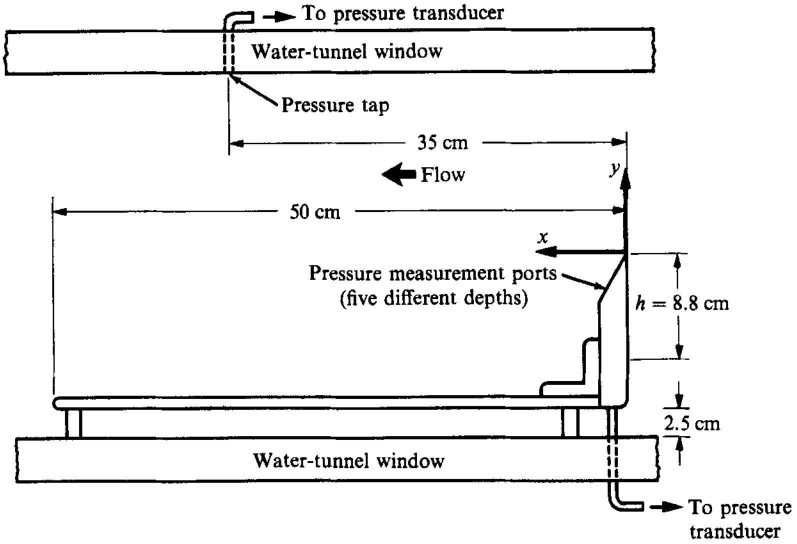

FIGURE 1. Diagram of the sharp-edged plate installed in the LTWT test section. The 2.5 cm stand-off distance allows boundary-layer fluid to escape underneath the plate to avoid contamination of the flow over the sharp edge.

The test body was a sharp-edged aluminium plate extending vertically into the flow, shown in figure 1. The tip of the 2.5 cm thick plate was chamfered to a 30° angle to give a clean sharp edge for flow separation. The plate spanned the full 0.3 m width of the test section and was sealed to the sidewalls to prevent leakage flow. A 2.5 cm stand-off above the floor of the test section prevented boundary-layer contamination of the shear layer, and a 50 cm long horizontal bypass plate separated the two flow regions. The sharp-edged plate blocked half of the oncoming flow, and the maximum velocity above the shear layer (U_L) was about 12 m/s. The minimum local static pressure above the shear region (p_L) was 1×10^4 Pa. The minimum cavitation index that could be achieved was $\sigma_L = (p_L - p_v)/(\frac{1}{2}\rho U_L^2) = 0.16$, where p_v and ρ are the water vapour pressure and density, respectively. The dissolved air content α was varied from saturation (about 15 p.p.m.) to as low as 3 p.p.m.

2.1. *Surface flow visualization*

Flow visualization studies were performed using paint droplets and tufts attached to the front surface of the sharp-edged plate. These studies clearly showed the location of the stagnation line on the front face of the plate, allowing measurement of the distance h from the stagnation line to the sharp-edge separation point, which was determined to be 8.8 cm, independent of U_L over the range 6 to 12 m/s. This characteristic lengthscale was used in determining the body Reynolds number and as a normalization factor.

2.2. *Cavitation inception testing*

Inception testing was made visually, using stroboscopic illumination. The primary goal was to determine the pressure required to initiate cavitation for specified test velocities and dissolved air contents. The tunnel velocity and air content was fixed and the water recirculated under steady non-cavitating conditions at high pressure. The cavitation index was then reduced at constant velocity by using a vacuum pump to lower the tunnel static pressure until the first traces of cavitation became visible. The pressure transducer reading was frozen at the moment of inception and recorded, together with the tunnel velocity, to allow calculation of the inception index. The location of the tap for making velocity and pressure measurements is shown in figure 1. Since the LTWT does not include a resorber, it was necessary to recirculate the water at atmospheric pressure (high steady-state σ) for at least ten minutes after each inception test in order to maintain a steady population of free-stream bubbles (see Katz 1984; Ooi 1985).

2.3. *Photographic studies*

Simultaneous top and side photographs were recorded by mounting cameras above and beside the test section; the shutter opening times were electronically synchronized with a high-speed flash unit (approximately 8 μs exposure). High-speed motion pictures were recorded at framing rates up to 2600 frames/s. Top, side and simultaneous views were recorded. Detailed frame-by-frame analysis of the motion picture film was performed using an NAC Film Motion Analyzer. The film speed for each frame was determined using timing marks automatically recorded on the edge of the film during exposure, and measured velocities were determined to be accurate to within 10%, based on tracking of free-stream particles in a constant-velocity stream. Fluctuations of the film registration in the camera led to an uncertainty in determination of object location of up to 3 mm in the cross-span views and about $\frac{1}{2}$ mm in the downstream location. The smallest objects that could clearly be identified and tracked in the high-speed motion pictures were about 1.5 mm diameter.

2.4. *Pressure fluctuation measurements*

The existence of large fluctuating pressure peaks in free turbulent flows is well known and plays a critical role in cavitation inception in these flows (Arndt & George 1979; Ooi 1981; Ooi & Acosta 1983). The mean pressure variations in a turbulent shear flow are often small, but the instantaneous peak pressures can vary significantly from the mean. Intrusive probes are unsuitable for detailed fluctuating pressure measurements because of the flow disturbances they cause, the fact that their size leads to spatially averaged pressure measurements, the directionality of their response, and the fact that vortex bursting can occur when a probe is placed in a vortex core. The concept of using specially 'tailored' air bubbles as Lagrangian pressure indicators was introduced by Ooi & Acosta (1983), and only a few key features of this technique will be presented here. The basic equation of bubble dynamics is the Rayleigh–Plesset equation which can be written as

$$p_\infty = \left[p_g + p_v - \frac{2S}{R} - \frac{4\nu\dot{R}}{R}\right] - \rho[R\ddot{R} + \tfrac{3}{2}\dot{R}^2], \tag{1}$$

where p_∞ is the free-stream static pressure, p_g the bubble gas partial pressure, p_v the vapour pressure, S the surface tension, R the bubble radius, ν the liquid kinematic viscosity, ρ the liquid density, and overdots indicate time differentiation. Ooi & Acosta (1983) show that (1) can be simplified by neglecting the inertial and viscous terms on the right-hand side when the bubble response time is short relative to the timescale of typical pressure fluctuations, so that the bubble responds instantaneously to the pressure fluctuations. The use of 'tailored' air bubbles involves injection of a uniform stream of dry air bubbles of known size into the flow, then monitoring the size of these bubbles as they pass through the pressure field of interest. The vapour pressure term can then be neglected, since the bubble initially contains only dry air, and the time between injection and measurement is short enough that evaporation to the bubble interior is negligible. Also, the bubble gas pressure term is known from bubble static equilibrium and the polytropic process, so (1) can be simplified to

$$p_x(t) = \left(p_0 + \frac{2S}{R_0}\right)\left(\frac{R_0}{R_x}\right)^{3\gamma} - \frac{2S}{R_x}, \tag{2}$$

where $p_x(t)$ is the instantaneous local pressure that a bubble at downstream position x is exposed to, R_0 and p_0 are bubble radius and pressure values established at a reference location, and R_x is the bubble radius at location x. Holograms are recorded of the flow field containing a large number of injected air bubbles of uniform initial size. The local instantaneous pressures p_x at numerous sites in the flow field can then be determined by measuring each bubble and using the local R_x values in (2). A Pockels cell Q-switched ruby laser was used as the coherent light source for Fraunhofer holography. The holocamera was also used for measurement of cavitation nuclei density distributions in another part of this study (O'Hern 1987).

Quasi-static bubble response requires that the bubble natural frequency be much greater than the exciting frequency, or frequency of the pressure fluctuations. The expected duration of pressure fluctuations in a turbulent jet at Reynolds numbers of approximately 2×10^5 is given by Ooi & Acosta (1983) to be of order 1 ms, based on detailed studies of turbulent jet pressure spectra. The dimensions of the present shear flow are larger than in the jet study above, and fluctuating pressure measurements were made at a Reynolds number of about 10^6. The duration of the pressure fluctuations in this flow are expected to be of the same order of magnitude, or at most one order of magnitude lower, than in the jet flows. A bubble of 70 μm radius has a characteristic response time of about 10 μs, an order of magnitude lower than the shortest expected pressure fluctuation period. A compromise between the quasi-static requirement and the bubble size needed for measurement accuracy leads to ideal injected bubble radii of 60 to 80 μm. The reference location was taken to be the flow region just above the back angled face of the sharp-edged plate. The reference static pressure p_0 at this location was measured, and the reference bubble radius determined by averaging the radii of several bubble images holographically recorded in this region. The bubble injector was a glass pipette of 45 μm internal diameter, fed by a constant-pressure supply of dry, filtered air. The bubble injector was attached to the front face of the test body, with the injector tip located on the tunnel centreline 1 cm below the sharp edge. Data holograms were recorded centred at the downstream location $x/h = 3.0$, and vertical location $y/h = 0.22$, in the nominal centre of the shear layer. Measurements of turbulent pressure fluctuations were made under non-cavitating conditions with $U_{\mathrm{L}} = 4.9$ m/s ($Re_{\mathrm{L}} = 2hU_{\mathrm{L}}/\nu = 9.57 \times 10^5$). The tunnel water was maintained at an air content just below saturation, and relatively high mean static pressure was maintained in order to avoid the occurrence of cavitation.

2.5. *Mean pressure measurements*

Static pressure was measured at several locations behind the sharp-edged plate. Pressure taps were located along the back of the plate and on the angled face (see figure 1), as well as on the upper surface of the horizontal bypass plate behind the sharp-edged plate.

3. Results and discussion

3.1. *Flow-field visualization*

Surface flow visualization using paint droplets and yarn tufts clearly established the two-dimensional nature of the flow on the front face of the test body. The oncoming stream splits at the front stagnation line, and laminar boundary layers accelerate from that line under favourable pressure gradients toward the top and bottom plate tips. The upper boundary layer separates at the sharp edge, forming a 'vortex layer' separating the free-stream flow above from the recirculating wake region below. The separation streamline undergoes very strong curvature for about one characteristic length h downstream. Distinct spanwise vortices roll up in the layer, and maintain their clarity beyond the end of the bypass plate, a downstream distance of about $x/h = 6$, at which point the shear flow becomes disturbed by mixing with the flow from beneath the bypass plate and observations were discontinued.

The turbulent mixing layer entrains fluid from the recirculating wake region, thus maintaining a base pressure p_B on the back of the plate which is lower than the local static pressure p_L. The average base pressure coefficient referenced to the local conditions p_L and U_L above the shear layer was -0.01 over the range $U_L = 3.4$ to 9.8 m/s.

3.2. *Cavitation flow visualization*

Figure 2 presents six side-view photographs of varying levels of cavitation in the shear layer, indicating the effect of cavitation number on the state of development of cavitation and providing an overall view of the vortex structure. The shear flow was fully turbulent for all conditions visualized ($1.2 \times 10^6 < Re_L < 2.1 \times 10^6$). The filamentous nature of the early stages of cavitation is quite distinct, and the cases with more fully developed cavitation clearly visualize the shear-layer turbulent structure.

Visual observations under stroboscopic light, as well as numerous photographic examinations at inception (see figure 3), have consistently demonstrated that inception occurs in the form of long, thin cavities oriented in the streamwise direction when viewed from above, and at roughly 45° to the mean flow direction when viewed from the side. These cavities indicate the low-pressure cores of the streamwise-oriented vortices of the shear layer, occurring in the high-strain braid regions between adjacent spanwise vortices. Inception was not observed in the spanwise vortices, indicating that the lowest pressures are found in the streamwise cores. At lower cavitation indices, more fully developed cavitation visualized both vortex types, as shown in figures 4 and 5. These photographs demonstrate that when both types of vortex structure are visible, the streamwise vortices are primarily confined to the braid region. It is not possible to tell from such a view whether the spanwise vortex cores are cavitating or whether they are made visible by entrainment of bubbles formed in the streamwise vortices. Finally, at very low cavitation numbers the full shear layer was visualized by cavitation bubbles, as shown in figures 6 and 7. These heavily cavitating conditions were used for most of the quantitative flow-field visualization analyses below.

High-speed motion pictures demonstrate significant variations in the cavitation level and overall appearance of the cavities over millisecond timescales. Figure 8 is a sequence of frames taken from one of the high-speed movies at inception, providing evidence of inception in longitudinal vortex cores; in the 2 ms between frames (*c*) and (*e*) two distinct cavities grow together to fill in the streamwise vortex core region. Other movies at inception have shown the growing cavity propagating *upstream* at speeds as high as 3.4 m/s against the free-stream velocity of 7.8 m/s as the core is 'filled in' by a cavity. Inception events occur at random throughout the shear layer, except that they are generally absent within the first plate height downstream. This random occurrence indicates that the streamwise vortex positions are not determined by such constant factors as possible imperfections of the sharp edge or mean flow

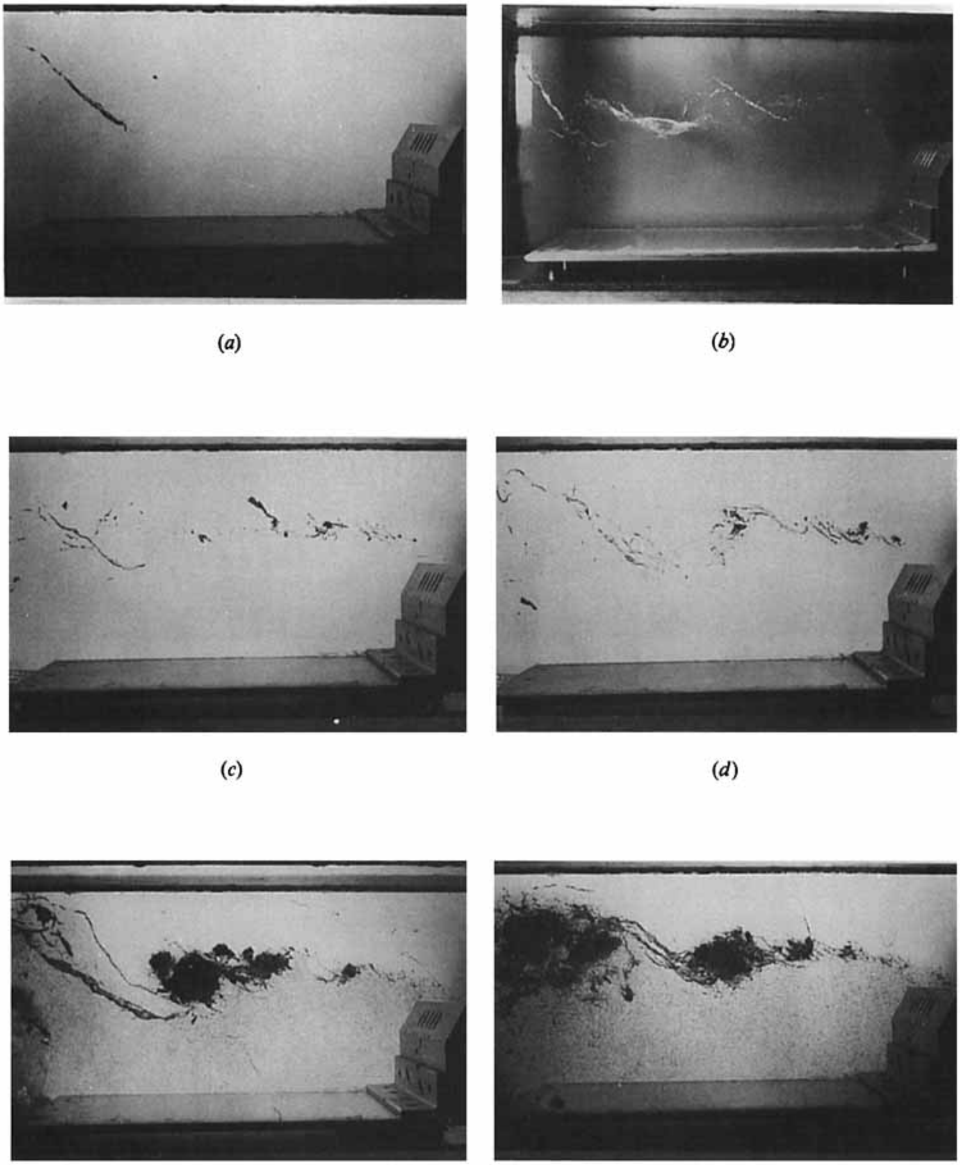

(*a*) (*b*) (*c*) (*d*) (*e*) (*f*)

FIGURE 2. Side-view photographs showing change in cavitation behaviour with decreasing cavitation index σ. A different lighting scheme was used for (*b*). (*a*) $Re_L = 1.5 \times 10^6$, $\sigma_L = 0.87$; (*b*) 2.0×10^6, 0.78; (*c*) 2.1×10^6, 0.65; (*d*) 2.1×10^6, 0.65; (*e*) 2.1×10^6, 0.41; (*f*) 2.1×10^6, 0.40.

non-uniformities. The appearance of cavitation did not qualitatively change after cleaning and rearranging the order of the flow conditioning screens, or after removing, anodizing and reinstalling the test body.

At very low cavitation indices, the spanwise vortices became visible close to the separating edge, appearing as straight linear cavities spanning the test section. Under these extreme conditions, inception was clearly observed in both the spanwise and the streamwise vortices, the first appearance of spanwise cavities occurring close to the sharp edge, and the streamwise cavities at a downstream distance of $x/h \approx 1$

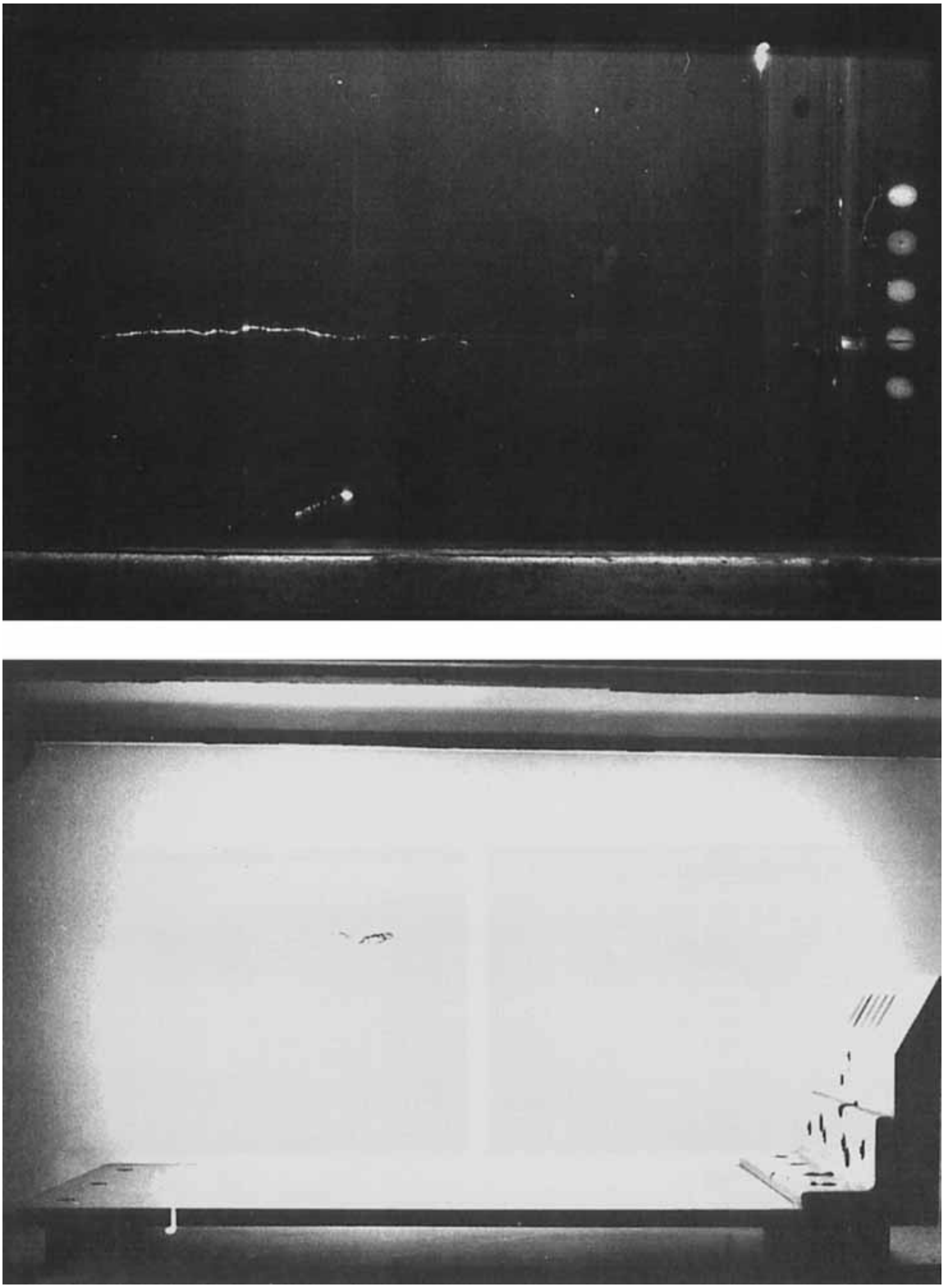

FIGURE 3. Simultaneous top and side photographs of shear-layer cavitation inception. $U_L = 7.81$ m/s, $\sigma_L = \sigma_i = 1.52$, $Re_L = 1.42 \times 10^6$.

to 3. The spanwise vortices had lost their sharp definition by the time they had convected about 15 cm downstream ($x/h = 1.7$), by which time the braid region was usually filled with thin, longitudinal cavities. Beyond about 20 cm downstream ($x/h = 2.3$), the spanwise vortices had grown considerably, and had lost the clear cavities filling their cores, appearing instead as large rotating bubble clouds. Figure 9 displays a sequence of frames taken from one of the high-speed movies showing a

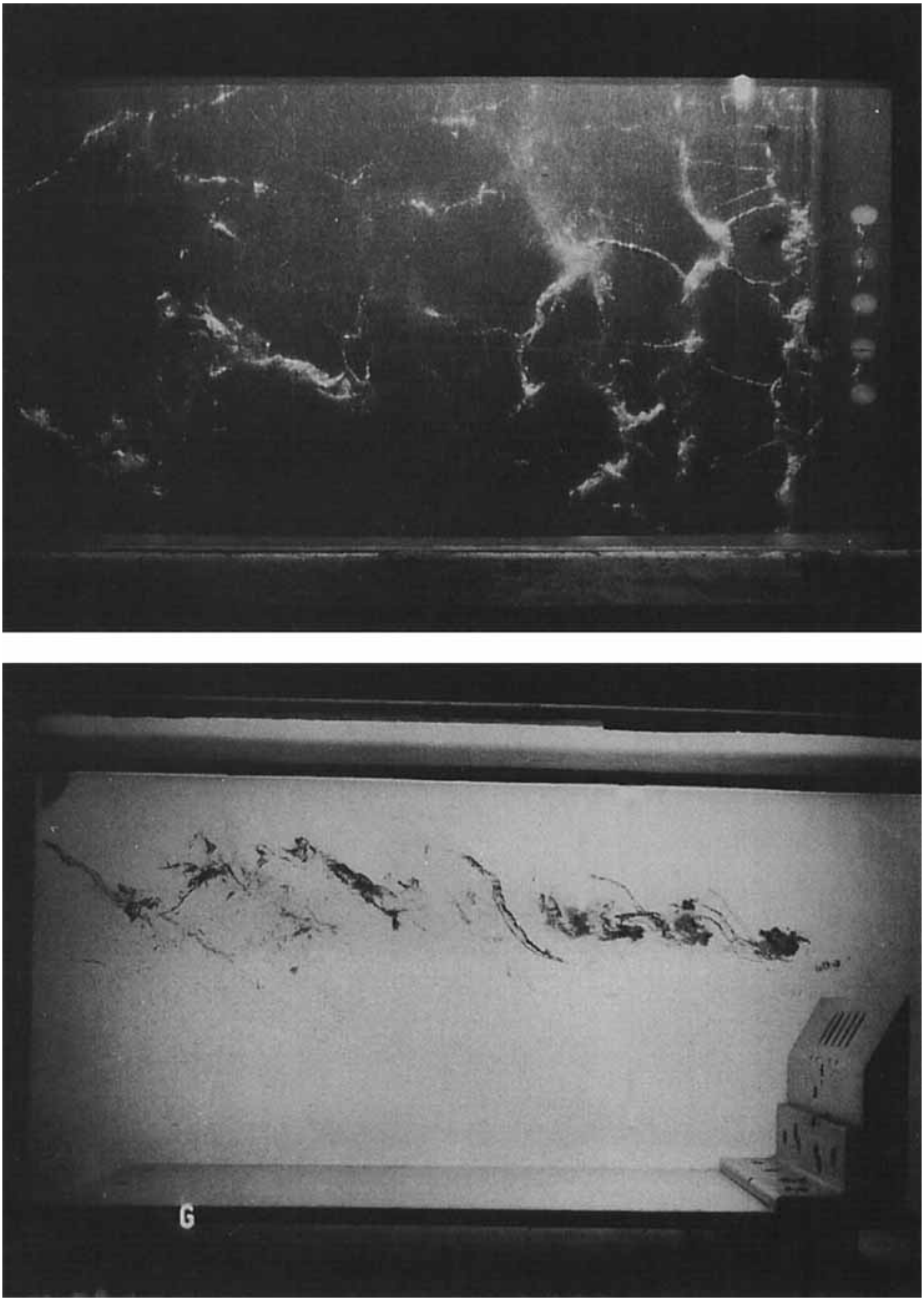

FIGURE 4. Simultaneous top and side photographs of early stage of cavitation in the shear layer. $U_{\mathrm{L}} = 11.38$ m/s, $\sigma_{\mathrm{L}} = 0.65$, $Re_{\mathrm{L}} = 2.06 \times 10^6$.

fairly well-developed state of cavitation in which both vortex types can be seen. The growth of longitudinal vortices in the braid between spanwise vortices is evident, as indicated by the inception of several cavities in the braid during the 4 ms between frames (*e*) and (*f*) of this sequence.

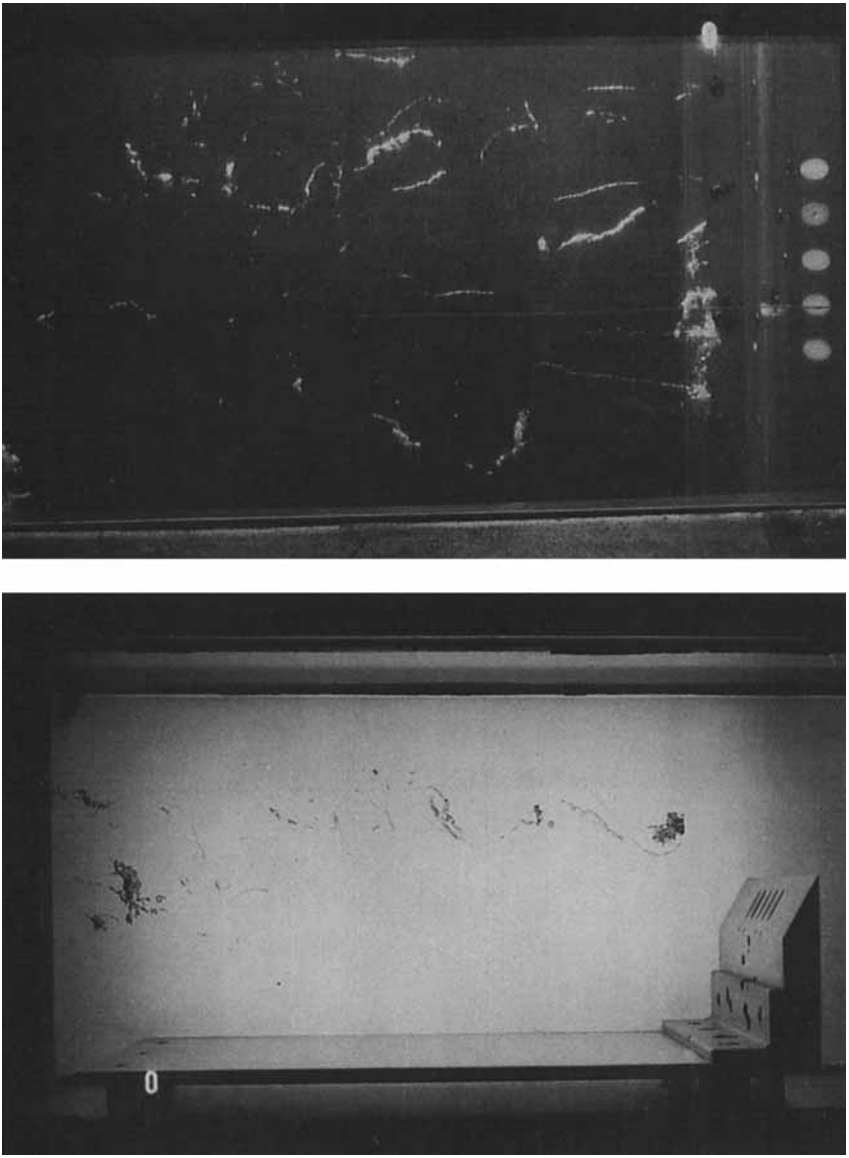

FIGURE 5. Simultaneous top and side photographs of early stage of cavitation in the shear layer. $U_L = 11.75$ m/s, $\sigma_L = 0.62$, and $Re_L = 2.13 \times 10^6$.

It should be pointed out that cavitation cannot be considered as a purely passive flow visualization technique. Franc & Michel (1983) have noted changes in vortex spacing and Strouhal number in the wake of a wedge due to changes in the cavitation index.

3.3. *Shear-layer growth rate*

Figure 10 presents the average shear-layer thickness measured at several fixed downstream stations. Growth rate analysis was made from the side-view motion pictures, with the shear-layer thickness visualized by cavitation bubbles. There is a large spread to the measured thickness values; the error bars in the figure indicate

FIGURE 6. Simultaneous top and side photographs of well-developed cavitation in the shear layer. $U_L = 10.14$ m/s, $\sigma_L = 0.39$, $Re_L = 1.84 \times 10^6$.

standard deviations from the mean thickness value for each downstream location. The average growth rate determined by fitting a straight line to the measured values is $\delta/h = 0.225(x/h + 0.25)$, also included in figure 10. This growth rate was verified by analysis of 20 long-exposure photographs, which indicated no systematic dependence

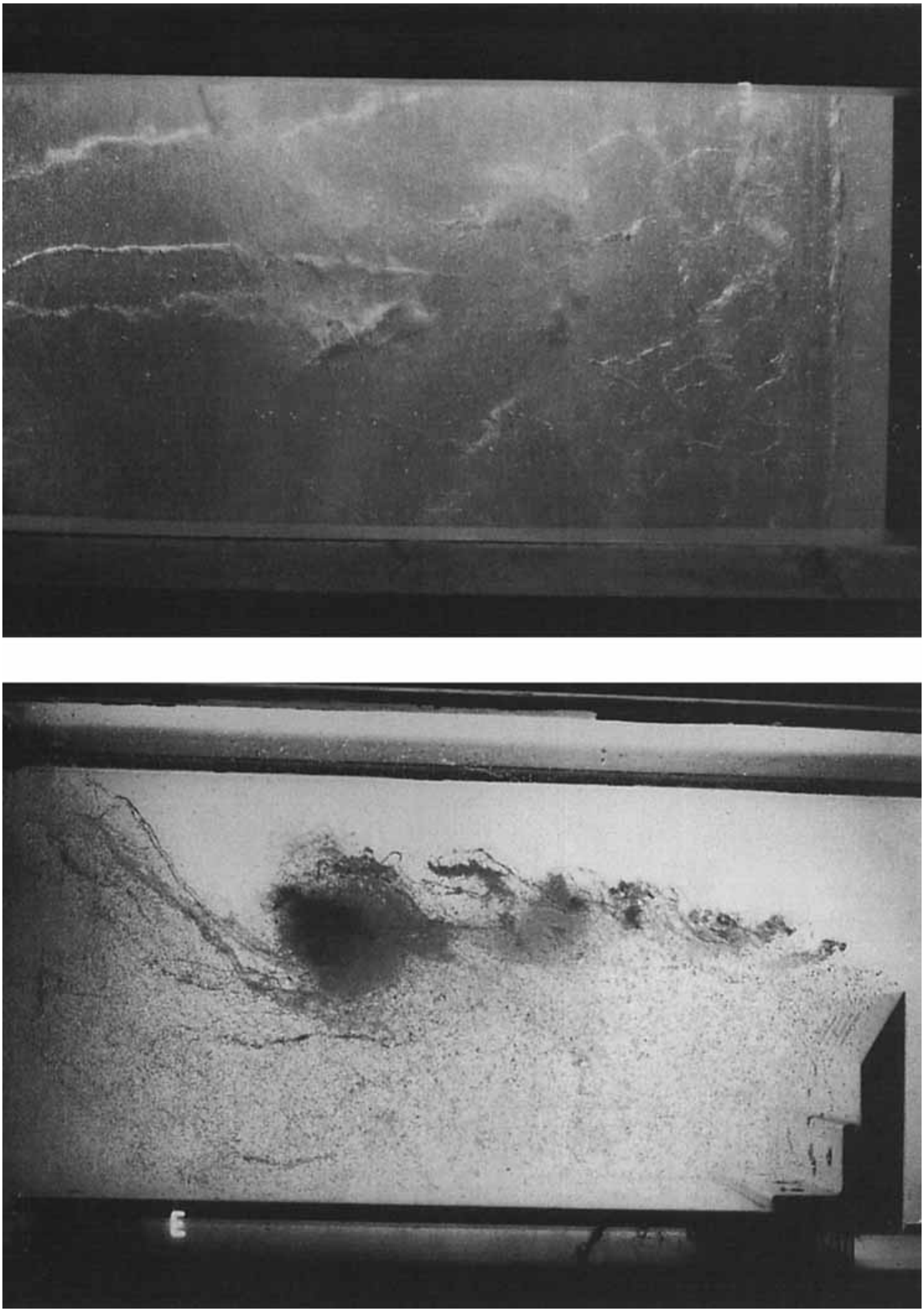

FIGURE 7. Simultaneous top and side photographs of well-developed cavitation in the shear layer. $U_{\mathrm{L}} = 10.14$ m/s, $\sigma_{\mathrm{L}} = 0.39$, $Re_{\mathrm{L}} = 1.84 \times 10^6$.

of the growth rate on free-stream velocity over the range $U_{\mathrm{L}} = 7.8$ to 11.3 m/s. The measured growth rate agrees fairly well with that measured by Kermeen & Parkin (1957) for the shear layer in the wake of a sharp-edged disk, given by $\delta/d = 0.26(x/d)$, where d is the disk diameter. Tollmien reported a growth rate $\delta/x = 0.255$ in a two-

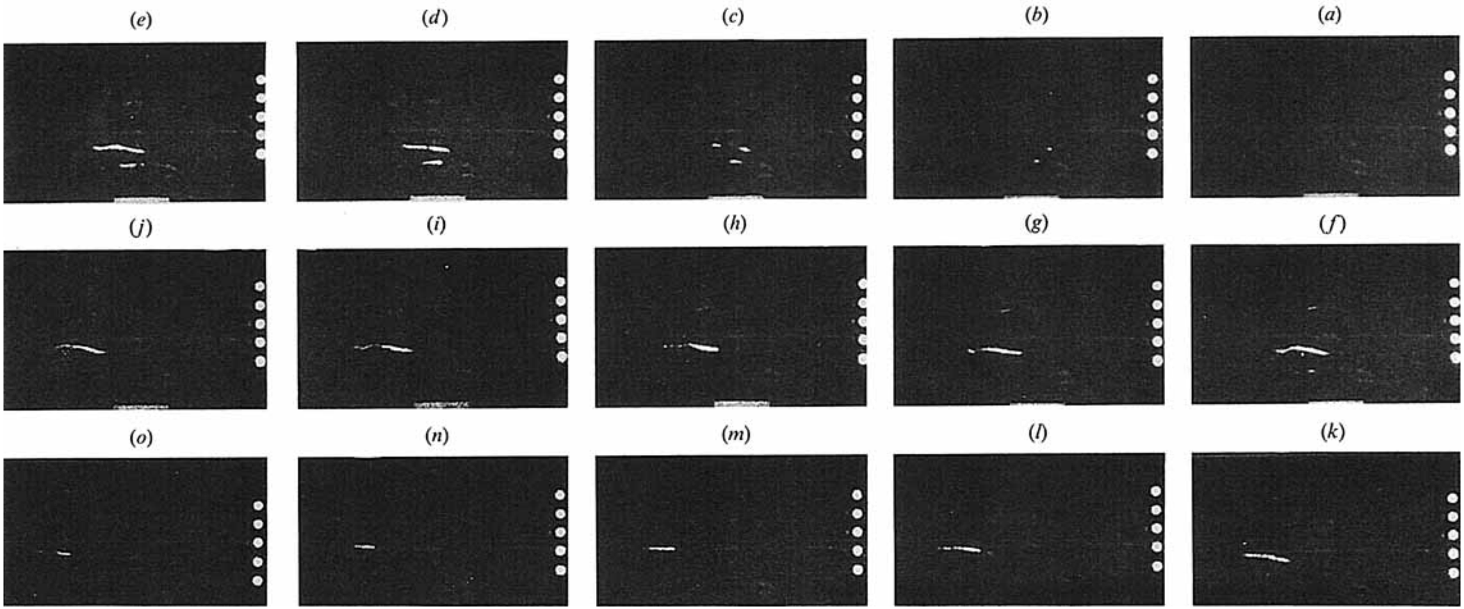

FIGURE 8. High-speed movie sequence showing top view of inception, growth and collapse of an axial cavity. Sequence runs from right to left as lettered. Flow direction is right to left. The steady streamwise line covering the full length of each frame is a scratch on the viewing window. Elapsed time between frames is 2 ms, exposure time is approximately 200 μs. $U_L = 9.5$ m/s, $\sigma_L = 0.88$, $Re_L = 1.84 \times 10^6$.

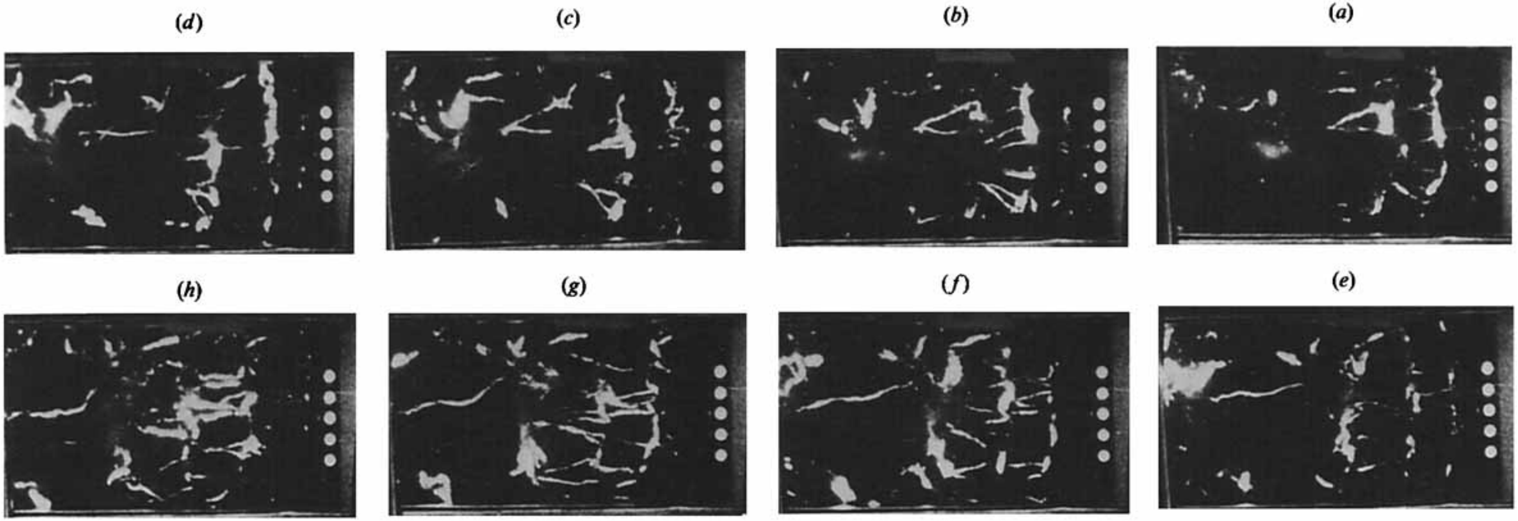

Figure 9. High-speed movie sequence showing top view of fairly heavy cavitation in the shear layer. Sequence runs from right to left as lettered. Flow direction is right to left. The steady streamwise line covering the full length of each frame is a scratch on the viewing window. Elapsed time between frames is 4.2 ms, exposure time is approximately 170 μs. $U_L = 11.60$ m/s, $\sigma_L = 0.63$, $Re_L = 2.26 \times 10^6$.

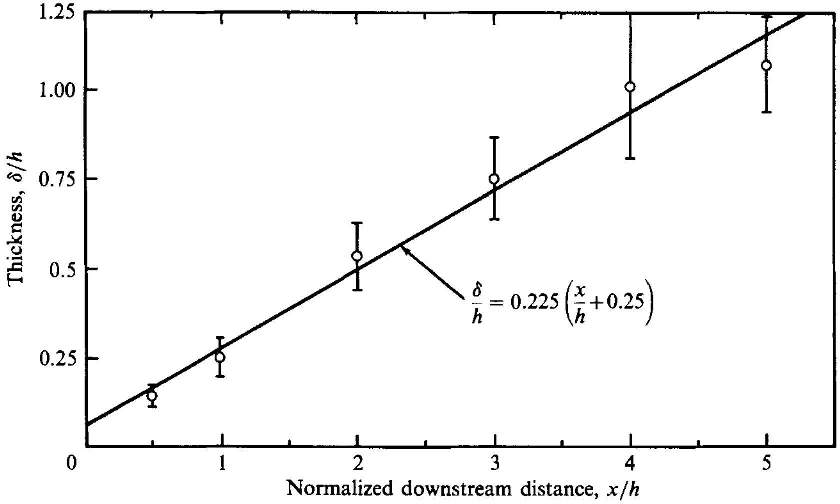

FIGURE 10. Shear-layer growth rate. 'Visual' thickness of layer measured from high-speed motion pictures at fixed downstream stations.

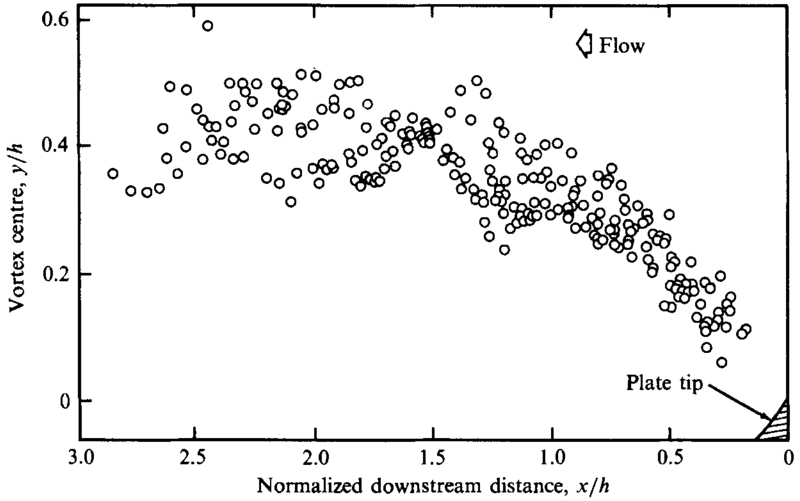

FIGURE 11. Trajectory of spanwise vortices in shear layer behind sharp-edged plate. $U_L = 10.76$ m/s, $\sigma_L = 0.37$, $Re_L = 1.95 \times 10^6$.

dimensional half jet (Goldstein 1965), and Batt (1977) reported a growth constant ($\delta/(x-x_0)$, where x_0 is the virtual origin) of 0.21 for the same type flow.

3.4. *Coherent structure*

Figure 11 shows the trajectories of spanwise vortices as they convect downstream. The data points indicate measured vortex centre locations from one of the high-speed motion pictures. High initial streamline curvature and downstream flattening are evident. Although the underlying flow fields are different, the overall appearance of the cavitating flows observed by Young & Holl (1966) and Franc & Michel (1983) in the wakes of various wedges are quite similar to the present observations. In all cases, spanwise vortices visualized by cavitation remain visible far downstream, but

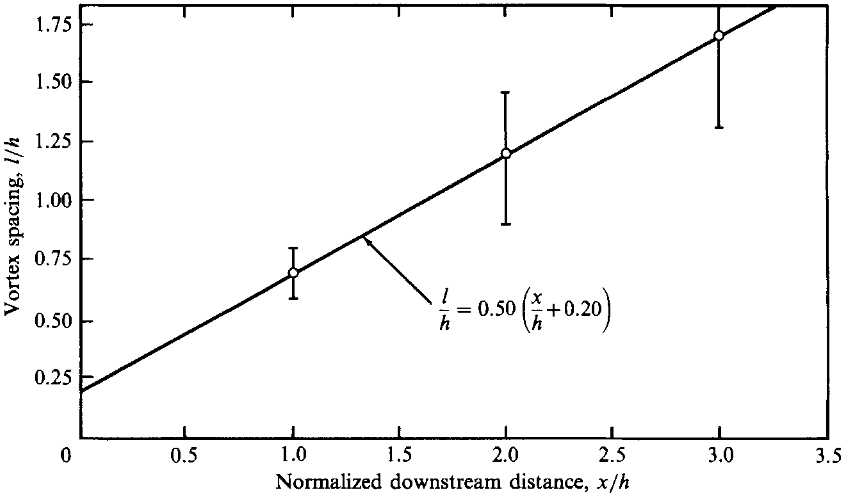

FIGURE 12. Spacing l of spanwise vortices as a function of downstream distance. Error bars indicate ± one standard deviation from the mean.

begin to lose their sharp appearance at some distance as bubbles become more dispersed within their cores.

In heavy cavitating flows, spanwise cavities became visible in the first 1 to 3 cm downstream from the sharp edge. Numerous cases of spanwise vortex pairing were observed. Persistence of the basic vortex structure through the pairing process was shown by the existence of well-defined cavities after pairing. Rotating spanwise cavities remained visible after pairing, but in most cases the bubbles visualizing their cores become more diffuse, making further downstream tracking difficult, particularly beyond the second and third pairing events. Pairing may not have been the only means of interaction of the spanwise vortices. Also indicated were coalescence of three vortices, 'tearing', and partial pairing as predicted by Moore & Saffman (1975) and observed by Dimotakis & Brown (1976).

The average spanwise vortex spacing l as a function of downstream position was measured in several high-speed motion pictures, defining l as the distance between adjacent braid/x-axis intersections (after Bernal 1981). Figure 12 displays vortex spacing measurements made in a single side-view motion picture at three fixed downstream locations, with the best line fit to the data being $l = 0.50(x-x_0)$, with $x_0 = 0.88$ cm. Dimotakis & Brown (1976) found values of the spacing constant $l/(\beta(x-x_0))$ in the range 0.4 to 0.5 for a plane two-stream mixing layer in water, where β is the velocity parameter $(U_1-U_2)/(U_1+U_2)$, with U_1 and U_2 the high and low stream speeds, respectively. Hernan & Jimenez (1982) found a value of 0.578 ± 0.193 by re-examining the films of Bernal (1981). In half-jets ($U_2 = 0$) Fiedler & Mensing (1985) found a value of 0.56 in an excited case, and Jimenez (1983) found 0.561 in an unexcited case. These spanwise spacing values are all in fairly good agreement with the present measured value.

Visible longitudinal cavities were not uniformly distributed across the span. Figure 13 shows the average spanwise spacing of longitudinal vortices as a function of downstream distance. There is a very large scatter in the data, but the mean spacing tends to increase with downstream distance. Previous investigations into the streamwise structure have also noted this trend (Bernal 1981; Jimenez 1983; Jimenez, Cogollos & Bernal 1985; Bernal & Roshko 1986; Lasheras *et al.* 1986).

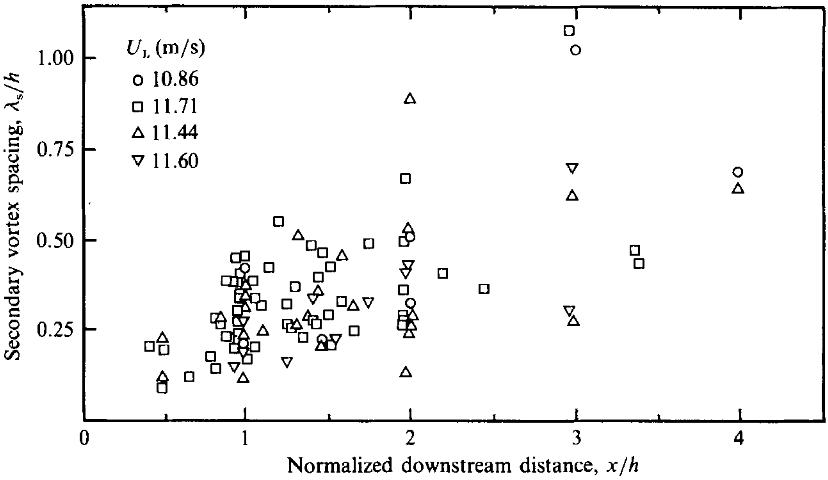

FIGURE 13. Average spanwise spacing of longitudinal vortices as a function of downstream distance.

Clearly, the flow examined in the present study has some fundamental differences from the more traditional two-stream plane shear layer, the major difference being the high initial streamline curvature just downstream of the sharp-edged plate. Inception was never observed in this high-curvature region, indicating that the lowest pressures occurred further downstream where the layer more closely resembled a plane mixing layer. The growth rates, spanwise vortex spacing and vortex shedding and passage frequencies were in fairly good agreement with those measured in plane mixing layers. Ho & Huerre (1984) discuss 'facility forcing', pointing out that scatter of up to 100 % is common between measurements of such shear-flow characteristics as growth rate and Strouhal number for examinations made in different test facilities, owing to variations in free-stream turbulence level and to details of the facility construction, which may lead to acoustic resonances at or near shear-layer instability frequency ranges. The differences between the measured characteristics of the present flow and those of plane mixing layers reported in the literature were relatively small in consideration of these large expected variations. In addition, most previous examinations of turbulent structure have been made in single-phase flows, while all but the inception observations of the present examination were made for well-developed stages of cavitation. Young & Holl (1966) and Franc & Michel (1983) have demonstrated that the presence of cavitation can strongly affect flow characteristics, so some of the observed differences may be attributed to the effect of heavy cavitation. However, the basic turbulent vortex structure of the present wake shear layer appears to be similar to that in the plane cases. High strain rates in the curved portion of the flow may provide additional amplification to the streamwise vortices, but the presence of these vortices is surely due to the same basic instability mechanism as in the plane mixing layer.

3.5. *Strength of streamwise vortices*

Streamwise vortex structures are not unique to plane mixing layers behind splitter plates. Velocity measurements made by Jimenez (1983) led to his recognition of the existence of 'longitudinal streamers' in a rectangular air half-jet. Ruderich & Fernholz (1986) observed longitudinal structures in the braid of the shear layer behind a sharp-edged plate. Clark & Kit (1980) noted an 'umbilical cord of vorticity'

Re_L	σ_L	x/h	r_c (mm)	Γ_s (m^2/s)	Γ_p (m^2/s)	Γ_s/Γ_p
1.39×10^6	1.52	2.7	0.5	0.02	1.06	0.02
1.39×10^6	1.52	3.4	2.7	0.12	1.06	0.09
1.39×10^6	1.52	3.6	0.8	0.03	1.34	0.02
1.39×10^6	1.52	3.7	0.8	0.03	1.40	0.02
1.39×10^6	1.52	4.6	0.8	0.03	1.69	0.02
1.59×10^6	0.92	1.8	1.1	0.04	0.86	0.05
1.59×10^6	0.92	2.2	0.5	0.02	1.02	0.02
1.59×10^6	0.92	3.4	0.5	0.02	1.47	0.01
1.59×10^6	0.92	4.3	1.1	0.04	1.83	0.02
1.59×10^6	0.92	4.7	2.5	0.10	1.97	0.05
1.59×10^6	0.92	5.0	4.3	0.16	2.07	0.08
1.68×10^6	1.47	2.9	0.9	0.05	1.36	0.03
1.68×10^6	1.47	2.9	1.4	0.07	1.35	0.06
1.68×10^6	1.47	3.1	1.0	0.05	1.45	0.04
1.68×10^6	1.47	3.2	0.5	0.02	1.49	0.02
1.68×10^6	1.47	4.2	0.6	0.03	1.87	0.02
1.68×10^6	1.47	4.4	0.6	0.03	1.96	0.02
1.85×10^6	1.02	3.2	0.48	0.02	1.62	0.01
1.85×10^6	1.02	3.2	0.48	0.02	1.64	0.01
1.85×10^6	1.02	4.3	0.93	0.04	2.10	0.02

TABLE 1. Relative strengths of streamwise and spanwise vortices in the shear layer. The streamwise vortex strength was determined using the Rankine vortex model and photographic measurements recorded near cavitation inception.

connecting the spanwise vortices in the wake of a sharp-edged orifice. Longitudunal vortices have also been detected in several cavitation studies, as will be discussed below.

The present cavitation observations have pointed out the dominant role of the streamwise vortices in the inception process in this flow. Estimates of the strength of these vortices were made by modelling them as Rankine vortices, allowing the vortex strength to be determined from cavitation inception observations and measurements. A Rankine vortex of radius r_c and vorticity ω has strength $\Gamma_s = \pi\omega r_c^2$ and a core pressure p_c given by

$$p_c = p_\infty - \rho\left[\frac{\Gamma_s}{2\pi r_c}\right]^2. \tag{3}$$

If, at the moment of inception, the core pressure is assumed to be equal to the water vapour pressure, (3) can be rearranged to give

$$\Gamma_s = 2\pi r_c U_L[\tfrac{1}{2}\sigma_L]^{\frac{1}{2}}. \tag{4}$$

For a vortex core radius r_c taken equal to the radius of the visible cavity at inception, the vortex strength was determined by measuring the cavity radius from photographs or high-speed movies recorded at the moment of inception, such as those shown in figures 3 and 8. These results were then applied in (4), along with the inception index and local velocity data measured at the time the photograph or movie was recorded. Representative results of such analyses are presented in table 1, which also includes estimates of the expected strength Γ_p of a spanwise ('primary') vortex if it were located at the same downstream location as the streamwise vortices used in determining the Γ_s values. The spanwise strength is given by $\Gamma_p = l(x)\,\Delta U$ (Moore & Saffman 1975; Bernal 1981), where $l(x)$ is the mean spanwise vortex spacing. Complete results are given in O'Hern (1987).

Several assumptions were made in estimating the strength values listed in table 1; the vortex core pressure at inception was assumed equal to the liquid vapour pressure, neglecting any gas pressure component, and the vortex core size was assumed equal to the measured cavity size, which should be accurate to within a proportionality factor. In addition, some of the photographs used to measure r_c were taken at conditions that were close to, but not precisely at, the moment of inception. In determining the strength of the spanwise vortices, it was necessary to use the free-stream velocity U_L as a measure of the velocity difference across the shear layer, since the velocity of the recirculating region beneath the shear layer was not measured. However, measurements of the convection velocity of spanwise vortices indicated that the recirculation velocity was about $0.2U_L$, so the spanwise vortex strengths could be as much as 20% higher than those listed in table 1. Because of these assumptions, the listed vortex strength values should be considered as order-of-magnitude estimates. This is also the reason that a simple Rankine vortex model was selected; further refinement of the vortex model would not improve the results significantly. Nevertheless, these results are unique in providing semi-empirical estimates of the streamwise vortex strength.

The results shown in table 1 indicate that the strength of streamwise vortices is always less than 10% of the spanwise strength ($\Gamma_s/\Gamma_p \leqslant 0.1$). Jimenez *et al.* (1985) estimated a relative strength of $\Gamma_s/\Gamma_p = 0.61 \pm 0.79$. Their scatter is very large, but the mean value indicates streamwise vortex strengths much larger than were estimated in the present study. Measurement of the thickness of the braid region, used in the calculations of Jimenez *et al.*, could not be made in the present study so direct comparison was not possible. Ashurst & Meiburg (1988) performed numerical simulations of the plane shear layer using discrete-vortex dynamics. Their results indicate that the strength ratio estimated by Jimenez *et al.* may have been high since it was based on the interface shape rather than on direct vorticity measurements. Their numerical simulations yield a strength ratio in the range $\Gamma_s/\Gamma_p = 0.2$ to 0.4 for the experimental configuration of Jimenez *et al.*, where unequal boundary layers from the top and bottom of the splitter plate form the mixing layer. For the single shear layer, more closely approximating the present experimental configuration, the numerical simulations of Ashurst & Meiburg (1988) yield a strength ratio $\Gamma_s/\Gamma_p \leqslant 0.12$ (estimated from their figure 6). These simulations appear to be in substantial agreement with the present strength estimates.

Jimenez (1983) determined that the strength of the streamwise vortices in a rectangular air half-jet was approximately equal to Γ_{p0}, the initial circulation of each wave of the Kelvin–Helmholtz instability. Estimates of Γ_{p0} in the present flow were made by using the expression for the growth rate of spanwise vortex spacing in the relation $\Gamma_p = l(x)\,\Delta U$, yielding an initial circulation of the order 0.1 $\mathrm{m^2/s}$. This value agrees fairly well with the estimated strengths of streamwise vortices listed in table 1, supporting the finding of Jimenez (1983) that $\Gamma_s \approx \Gamma_{p0}$.

3.6. *Turbulent pressure fluctuations*

The air-bubble injection technique was used to determine the magnitude of turbulent pressure fluctuations in the shear region. Holograms recorded at the injector tip indicated that the injected bubble size was very uniform, and that bubbles followed

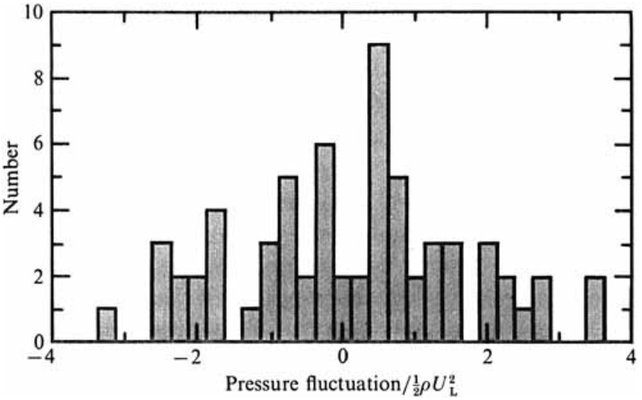

FIGURE 14. Normalized pressure fluctuation distribution. Polytropic constant $\gamma = \frac{4}{3}$.

the accelerating flow up the plate face. When bubbles reached the high-shear region at the sharp edge, many of them were sheared to an ellipsoidal shape, but bubble breakup was never observed. Those bubbles that were deformed as they entered the high-shear region recovered to a more spherical shape within a few centimetres downstream, well before their sizes were holographically recorded. The accuracy of bubble radius measurement during holographic reconstruction was better than 1 μm, leading to pressure determination accuracy of about 5%.

The pressure fluctuation measurements were made with $U_L = 4.9$ m/s and an injected bubble diameter of 147 μm. The three holograms analysed were found to contain spurious bubble images along with those of the injected bubbles of interest. A total of 90 bubbles was found at the downstream measurement site, rather than the 60 to 80 expected for the known injection rate. The problem of free bubbles in the tunnel water interfering with the pressure measurements had been anticipated and attempts were made to minimize their effect (O'Hern 1987). Rather than bubbles traversing the flow loop and re-entering the region of interest, the problem was more likely one of entrainment of injected bubbles immediately into the recirculating wake region. The high free-stream static pressure indicated by the full original measured distribution indicated that too many small bubbles had been counted. Therefore, small-bubble counts were selectively neglected in an attempt to recover the distribution due only to injected air bubbles. The goal was to recover the bubble distribution that indicated a mean static pressure close to the measured base pressure, while simultaneously reducing the total number of counts to that expected for the known injection rate. The 20 smallest bubbles, and 5 largest, were discarded to give a final distribution of 65 bubbles centred around a mean diameter of 162 μm with a standard deviation of 7 μm. Maximum deviations from the mean diameter were 151 μm and 181 μm, indicating peak instantaneous pressures of 64% to 137% of the mean indicated static pressure of 1.1×10^4 Pa. When normalized with the local dynamic pressure (above the shear layer), an r.m.s. pressure fluctuation of 153% of the local dynamic pressure was indicated, with peak pressure fluctuations of +344% and −336% of the local dynamic pressure. The normalized pressure fluctuation distribution is given in figure 14. In consideration of the fact that the bubbles remaining in the distribution were selected from a larger group, the exact numbers must be considered somewhat arbitrary, since they could be shifted by changing the bubble selection criteria. Therefore, the final result cannot be stated with more precision than that the pressure fluctuations were about ±300% of the free-stream

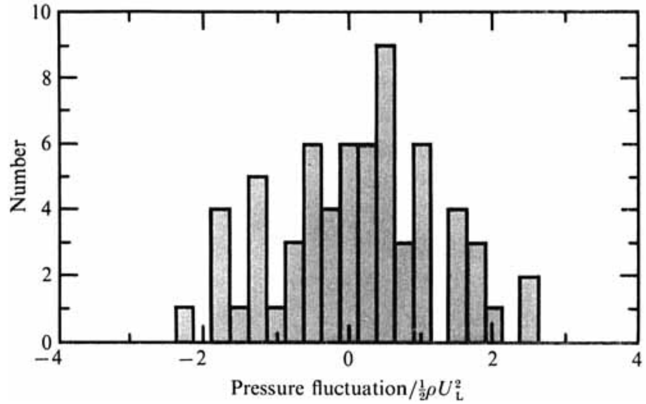

FIGURE 15. Normalized pressure fluctuation distribution. Polytropic constant $\gamma = 1.0$.

dynamic pressure. The bubble entrainment problem prevented fluctuating pressure measurements at higher velocities. The calculations above assumed a polytropic constant $\gamma = \frac{4}{3}$. Assumption of an isothermal case ($\gamma = 1.0$) leads to a slightly lower intensity of pressure fluctuations ($\approx \pm 250\%$). The histogram of normalized pressure fluctuation values for the isothermal case is given in figure 15.

The pressure fluctuation results of Ooi & Acosta (1983) in a turbulent jet shear layer are the only comparable ones reported to date. The measured pressure peaks in that investigation were as high as $+160\%$ and -120% of the jet dynamic pressure, the fluctuations fitting a Gaussian distribution slightly skewed toward positive pressures. The r.m.s. pressure fluctuations were 64% of the jet dynamic pressure, 4 to 8 times higher than any previously reported, possibly because previous measurements had been made with transducers that were larger than the bubble 'pressure sensors' and so tended to spatially average the pressure signal (Ooi 1981). The present results also demonstrate very large pressure fluctuations, with r.m.s. values up to 150% of the local dynamic pressure and peaks on the order of ± 3 times the local dynamic pressure. The uncertainty in the present measurements is considerably higher than in the investigation made by Ooi, however.

The uncertainty in the present results is high because of the limited number of measurements and because the presence of a recirculating wake region restricted the applicability of the air bubble injection technique. Even if it had been possible to isolate and measure only injected bubbles at the downstream measurement location, several potential error sources exist in this pressure measurement technique. First, it is not clear what value to use for the polytropic index γ, although both the present results and those of Ooi (1981) show that this choice does not have a dominant effect on the calculated pressure fluctuation values (see figures 14 and 15). Second, the bubbles are strongly sheared when they enter the turbulent shear region, so their reconstructed images often project an ellipsoidal cross-sectional area when recorded downstream. Ooi (1981) has shown that ellipsoidal bubbles remain valid pressure indicators.

Use of the air-bubble injection technique to find the peak pressures in the flow relies on the assumption that some of the injected bubbles are exposed to the low-pressure cores of streamwise vortices. The odds of finding an injected bubble in a vortex core is fairly low since at the downstream location of hologram recording only 4 to 6 streamwise vortices were typically visible across the span, so a stream of injected bubbles would at best encounter one of them. Nevertheless, the large indicated pressure fluctuations imply that at least some of the bubbles may have encountered one of the vortex cores.

The calculated peak pressure values are quite large and therefore very significant in terms of cavitation inception. The minimum pressure in the flow is given by the maximum negative pressure deviation from the mean, i.e. $p_{\min} = p_B - p'$, where p_B is the base pressure and p' is the maximum fluctuation. The local cavitation inception index σ_L is based on the mean local flow velocity and pressure values, so the minimum pressure coefficient in the flow at the moment of inception can be expressed as

$$\frac{p_{\min}-p_v}{\frac{1}{2}\rho U_L^2} = C_{pb} + \sigma_L - \frac{p'}{\frac{1}{2}\rho U_L^2}, \tag{5}$$

where C_{pb} is the base pressure coefficient based on the local pressure and velocity, which was on the order of -0.01 over all flow velocities for the present tests. The measured magnitudes of the negative pressure peaks, on the order of 3 times the local dynamic pressure, are clearly strong enough to explain cavitation inception at relatively large values of σ_L. Instantaneous pressure measurements cannot provide the spectrum of pressure fluctuations, so the duration of the pressure peaks is unknown. In particular, the question arises as to whether bubbles and other nuclei are exposed to the low pressures for a sufficient time period to allow cavitation to occur. However, since the low-pressure peaks are assumed to correspond to streamwise vortex cores, they are expected to persist for a significant time relative to the bubble response time. High-speed motion pictures showed longitudinal vortex lifetimes on the order of 100 ms, very long relative to typical bubble response times.

3.7. *Cavitation inception*

Visual and photographic observations clearly demonstrated that cavitation occurred only in the shear layer behind the sharp-edged plate. Newly formed bubbles collapsed when they reached a higher pressure region downstream. Cavity growth and collapse were generally explosive; cavity wall growth rates up to 18 m/s, and collapse rates up to 8.5 m/s, were measured. All of the flows visualized were fully turbulent, and the appearance of cavitation had significant instantaneous variations even for fixed mean flow conditions. As demonstrated in figures 3 and 8, the first cavities at inception were long thin 'strings' oriented in the longitudinal direction, presumably indicating the coincidence of a cavitation nucleus with a low-pressure longitudinal vortex core. Inception occurred at random sites throughout the shear layer, although generally at least one plate height downstream rather than near the sharp edge. Inception was never seen to occur in the corner vortices upstream of the sharp-edged plate.

The dominant effect of the streamwise vortex structure on cavitation inception is not unique to the present flow configuration. Van der Muelen (1980) noted the 'irregular threadlike appearance of cavitation' in the separated flow past hydrofoils. Inception in the separated shear layer around blunt circular cylinders studied by Katz (1984) clearly occurred in thin, axially oriented vortices, which remained visible even when heavier cavitation filled in the circumferential vortices. Photographs of shear-layer cavitation in Kermeen & Parkin (1957) provide evidence that early stages of cavitation in the wake of a sharp-edged disk took place in similar thin, streamwise-oriented structures. The study of vortex shedding in the wake of wedges by Franc & Michel (1983) showed cavitation in both the large shed vortices as well as in the thin 'three-dimensional rotational filaments' connecting them.

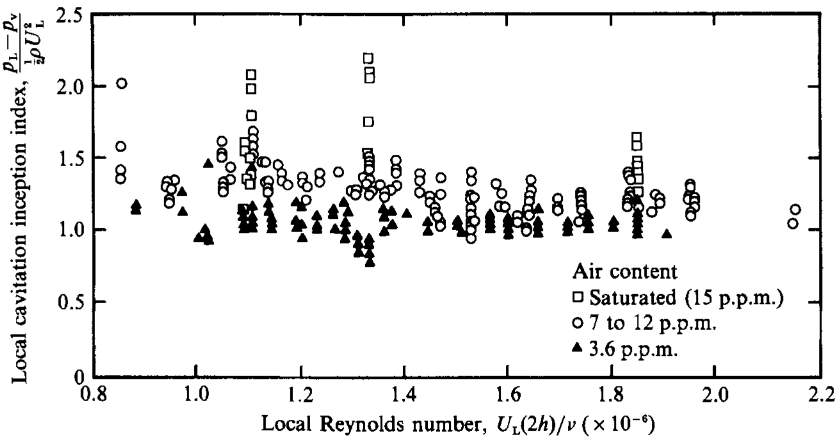

FIGURE 16. Cavitation inception indices in the shear layer. Note the strong dependence of inception index on dissolved air content.

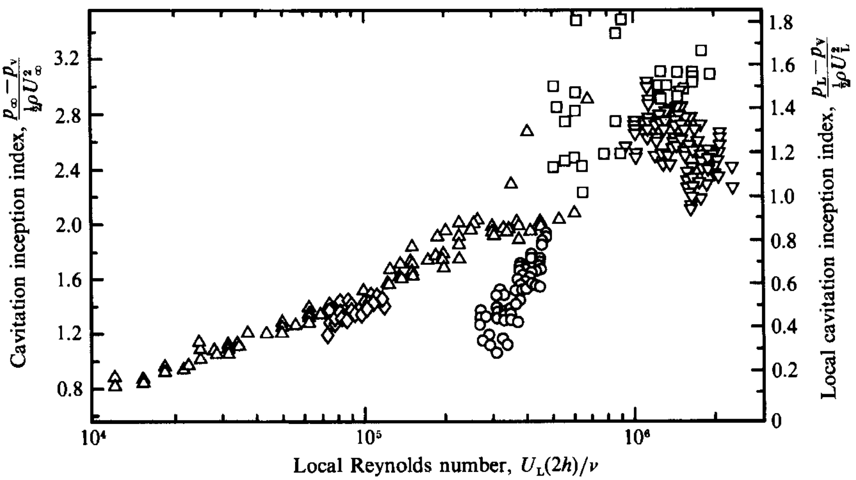

FIGURE 17. Comparison of the data of figure 16, at $\alpha = 9$–12 p.p.m. (▽), with inception measurements on sharp-edged disks by Kermeen & Parkin (1957) (△) and Arndt (1978) (□), and on $\frac{1}{2}$ in. (◇) and 2 in. (○) blunt circular cylinders at $\alpha = 10$ p.p.m. by Katz (1984).

3.8. *Inception indices*

Local cavitation inception indices are plotted against the body Reynolds number in figure 16. The lengthscale in the Reynolds number is $2h$, or twice the distance between the test body stagnation and separation lines, in order to allow direct comparison of the present results to those made on axisymmetric bodies. The present inception index values are numerically large, but do not show any clear Reynolds-number dependence. The data scatter, and the narrow range of velocities under which inception can be achieved in the tunnel, preclude determination of any universal trend.

Figure 17 compares the present results at high air content to those of Kermeen & Parkin (1957) and Arndt (1978) behind sharp-edged disks and those of Katz (1984) in the flow around flat-faced circular cylinders. The present results extend the upper Reynolds-number bound of the data in this plot. The local cavitation inception index is based on conditions above the shear layer in the present results, while the values of the inception index in the other experiments are based on the pressure and velocity at infinity. In order to compare the results, the axes of figure 17 were adjusted according to the relation

$$\sigma_L = \frac{\sigma_i + C_{pb}}{1 - C_{pb}}, \tag{6}$$

where C_{pb} is the minimum base pressure coefficient, which was measured by both Kermeen & Parkin (1957) and Katz (1984) to average -0.6. The values of the Reynolds number were also adjusted to the local velocity.

The data of figures 16 and 17 show that although the present results do not, by themselves, display a clear trend with velocity (Reynolds number), they are in general agreement with the commonly observed overall increase in inception index with increasing Reynolds number. A large scatter can be seen in the data, primarily because the onset of cavitation (in any type of flow) requires the coincidence of at least two events, a low enough pressure (occurring in the streamwise vortex cores in this flow) and a free-stream cavitation nucleus of such size that it becomes unstable at the local pressure (Katz & O'Hern 1986).

The occurrence of inception in the cores of longitudinal vortices may provide an explanation for the commonly observed dependence of the inception index in shear flows on the Reynolds number. Although the strength of streamwise vortices and their dependence on flow conditions have not yet been firmly established, several important aspects of their behaviour have recently been elucidated by Bernal (1981), Bernal & Roshko (1986), and Lasheras *et al.* (1986). The shear layer is unstable to three-dimensional disturbances, with flow perturbations upstream acting to trigger the instability. Bernal has demonstrated a velocity dependence of the three-dimensional instability amplification process, in that the downstream location of the 'streak' visibility threshold can be shifted by changing the velocity level or the velocity ratio. The number of axial vortices and their spanwise pattern also changes with velocity. This velocity-dependent behaviour indicates that the vortex strength increases with velocity, so cavitation occurring in these vortex cores would be expected to occur more readily at higher velocities, possibly explaining the observations of increasing cavitation index with increasing Reynolds number.

3.9. *Scaling laws for shear flows*

The key parameters controlling cavitation inception in any flow are the susceptibility of the liquid, that is the concentration, size distribution, and type of nuclei available, and the characteristics of the pressure field to which the nuclei are exposed. In turbulent flows, the magnitude and spectra of the minimum pressure peaks are needed, along with the nuclei distributions, in order to define the conditions at inception.

Nuclei availability plays an important role in cavitation scaling, and the dissolved air content is well known to characterize bubble nuclei concentrations. The present inception results in figure 16 demonstrate that at a fixed velocity the water containing the highest air content will tend to cavitate most readily. Therefore, the detailed nuclei content, or at least the dissolved air content, must be included in cavitation scaling laws. Experimental data and a complete discussion of nuclei availability in the present tests is given in O'Hern (1987).

The cavitation index σ is the standard parameter used to characterize cavitation behaviour. However, difficulties arise when applying σ to characterize the inception conditions of shear flows, since a strong Reynolds-number dependence has commonly been observed. The results of Kermeen & Parkin (1957) provide inception indices for disks of various diameters and free-stream velocities, and clearly show that the Reynolds number is a valid parameter to collapse the experimental data to a single curve (as included in figure 17). Their data indicate a possible levelling off of the inception index at the high-Reynolds-number limit ($\approx 10^6$), leaving only a size dependence. The narrow range of Reynolds numbers covered during inception tests, and the scatter of the data, prevent determination of any particular trend. Size dependence could not be investigated with the present test apparatus. The possible effect of streamwise vortices on Reynolds-number dependence of the inception index was discussed above for those flows in which streamwise vorticity plays a dominant role in the inception process.

One of the limitations of the cavitation index as commonly defined, based on mean free-stream velocity and pressure, is that it does not include the fluctuating pressure components needed to explain cavitation behaviour in turbulent flows. Equation (5) shows that fluctuations can cause a minimum flow pressure significantly lower than the mean free-stream value used in determining σ.

4. Summary and conclusions

Cavitation phenomena were studied in the turbulent shear flow behind a sharp-edged plate at Reynolds numbers up to 2×10^6. Two distinct types of vortex motion were evident in the shear layer, the spanwise and streamwise vortices. The streamwise vortices control cavitation inception, indicating that the lowest pressures occur in the cores of these vortices. Inception occurred at random locations throughout the shear layer, although not in the high-curvature region just downstream of the sharp-edged plate. No clear downstream or spanwise location of most probable occurrence of inception could be defined. More fully developed cavitation visualized both vortex structures, with the streamwise cavities primarily confined to the braid regions between the spanwise vortices. A Rankine vortex model showed that the strength of the streamwise vortices was always less than 10% of that of the spanwise vortices. Overall flow characteristics including growth rate and vortex spacing displayed a scatter characteristic of turbulent flows but indicated that the present shear layer is similar to other free turbulent shear flows, including the plane two-stream mixing layer.

Air-bubble injection was used to measure fluctuating pressure peaks in the non-cavitating shear layer. Very large pressure fluctuations were measured, with positive and negative peaks as high as 3 times the local dynamic pressure. The observed magnitude of the negative pressure peaks is sufficient to explain cavitation inception occurring at large values of the inception index. However, there is a large experimental uncertainty due to the limited number of measurements and to the fact that the present flow, with its recirculating region, is not well suited to the air-bubble injection technique.

Cavitation inception indices display a strong dependence on the air content and thus on the availability of free-stream bubbles as cavitation nuclei. The Reynolds-number scaling effect on the inception indices was examined at higher values of the Reynolds number than previously reported. The narrow range of Reynolds numbers covered during inception tests, and the scatter of the data, prevented determination of a clear relation between the inception indices and the velocity (or Reynolds number), although the present data are generally consistent with the commonly observed trend of increasing inception index with increasing Reynolds number.

Bernal (1981) demonstrated that streamwise vortex strength may be velocity-dependent. This observation, along with the present results indicating the importance of these vortices in the cavitation inception process, may be the key to explaining the commonly observed Reynolds-number dependence of the inception index.

Special thanks to Professor A. J. Acosta, whose insight and guidance were irreplaceable in the course of this work. Professor J. Katz of Johns Hopkins University was a valuable colleague during the early stages of this research. I would also like to give special acknowledgement of the financial support of this research provided by the Office of Naval Research and the Naval Sea Systems Command General Hydromechanics Research Program administered by the David W. Taylor Research Center under contract N000167-85-K-0165. This support is deeply appreciated. Special thanks to Dr T. T. Huang of DTRC for his personal involvement and interest in this work.

REFERENCES

Arndt, R. E. A. 1978 Investigation of the effects of dissolved gas and free nuclei on cavitation and noise in the wake of a sharp-edged disk. *Joint IAHR/ASME/ASCE Symp. on Fluid Machinery, Fort Collins, Colorado.*

Arndt, R. E. A. & George, W. K. 1979 Pressure fields and cavitation in turbulent shear flows. *12th Symp. on Naval Hydrodynamics, Washington, DC.* National Academy Press.

Ashurst, W. T. & Meiburg, E. 1988 Three-dimensional shear layers via vortex dynamics. *J. Fluid Mech.* **189**, 87–116.

Batt, R. G. 1977 Turbulent mixing of passive and chemically reactive species in a low-speed shear layer. *J. Fluid Mech.* **82**, 53–95.

Bernal, L. P. 1981 The coherent structure of turbulent mixing layers, I. Similarity of the primary vortex structure, II. Secondary streamwise vortex Structure. Ph.D. thesis, Graduate Aeronautical Laboratories, California Institute of Technology.

Bernal, L. P. & Roshko, A. 1986 Streamwise vortex structure in plane mixing layers. *J. Fluid Mech.* **170**, 499–525.

Brown, G. L. & Roshko, A. 1974 On density effects and large structure in turbulent mixing layers. *J. Fluid Mech.* **64**, 775–816.

Clark, J. A. & Kit, L. 1980 Shear layer transition and the sharp-edged orifice. *Trans. ASME* J: *J. Fluids Engng* **102**, 219–225.

Dimotakis, P. E. & Brown, G. L. 1976 The mixing layer at high Reynolds number: large-structure dynamics and entrainment. *J. Fluid Mech.* **78**, 535–560.

Fiedler, H. E. & Mensing, P. 1985 The plane turbulent shear layer with periodic excitation. *J. Fluid Mech.* **150**, 281–309.

Franc, J. P. & Michel, J. M. 1983 Two- and three-dimensional rotational structures in the cavitating turbulent wake of a wedge. Presented at *the Fourth Symp. on Turbulent Shear Flows, Karlsruhe, Germany.*

Gates, E. M. 1977 The influence of freestream turbulence, freestream nuclei populations and a drag-reducing polymer on cavitation inception on two axisymmetric bodies. Ph.D. thesis, California Institute of Technology, *Rep.* 183-2.

Goldstein, S. (ed.) 1965 *Modern Developments in Fluid Dynamics*, Volume II, p. 599. Dover.

Hernan, M. A. & Jimenez, J. 1982 Computer analysis of a high-speed film of the plane turbulent mixing layer. *J. Fluid Mech.* **119**, 323–345.

Ho, C. M. & Huerre, P. 1984 Perturbed free shear layers. *Ann. Rev. Fluid Mech.* **16**, 365–424.

Jimenez, J. 1983 A spanwise structure in the plane shear layer. *J. Fluid Mech.* **132**, 319–336.

Jimenez, J., Cogollos, M. & Bernal, L. 1985 A perspective view of the plane mixing layer. *J. Fluid Mech.* **152**, 125–143.

Katz, J. 1984 Cavitation phenomena within regions of flow separation. *J. Fluid Mech.* **140**, 397–436.

Katz, J. & O'Hern, T. J. 1986 Cavitation in large scale shear flows. *Trans. ASME* J: *J. Fluids Engng* **108**, 373–376.

Kermeen, R. W. & Parkin, B. R. 1957 Incipient cavitation and wake flow behind sharp-edged disks. *California Institute of Technology, Hydrodynamics Lab Rep.* 85-4.

Lasheras, J. C., Cho, J. S. & Maxworthy, T. 1986 On the origin and evolution of streamwise vortical structures in a plane, free shear layer. *J. Fluid Mech.* **172**, 231–258.

Moore, D. W. & Saffman, P. G. 1975 The density of organized vortices in a turbulent mixing layer. *J. Fluid Mech.* **69**, 465–473.

O'Hern, T. J. 1987 Cavitation inception scale effects I. Nuclei distributions in natural waters II. Cavitation inception in a turbulent shear flow. Ph.D. thesis, California Institute of Technology, *Rep. Eng.* 183.15.

Ooi, K. K. 1981 Scale effects on cavitation inception in submerged jets. Ph.D. thesis, California Institute of Technology, *Rep.* 183-6.

Ooi, K. K. 1985 Scale effects of cavitation inception in submerged water jets: a new look. *J. Fluid Mech.* **151**, 367–390.

Ooi, K. K. & Acosta, A. J. 1983 The utilization of specially tailored air bubbles as static pressure sensors in a jet. *ASME* Paper 83-FE-34.

Ruderich, R. & Fernholz, H. H. 1986 An experimental investigation of a turbulent shear flow with separation, reverse flow, and reattachment. *J. Fluid Mech.* **163**, 283–322.

Van der Muelen, J. H. J. 1980 Boundary layer and cavitation studies of NACA 16-012 and NACA 4412 hydrofoils. *13th Symp. on Naval Hydrodynamics, Sasakawa Hall, Tokyo.* Tokyo: Shipbuilding Research Association of Japan.

Winant, C. D. & Browand, F. K. 1974 Vortex-pairing: the mechanism of turbulent mixing layer growth at moderate Reynolds number. *J. Fluid Mech.* **63**, 237–255.

Young, J. O. & Holl, J. W. 1966 Effects of cavitation on periodic wakes behind symmetric wedges. *Trans. ASME* D: *J. Basic Engng* **88D**, 163–176.